Title: Estimating the Seepage Effect of SC-CO2 and Water Fracturing with a Steady-state Flow Model: Consider Capillary and Viscous Forces in Pore Scale

Abstract: Supercritical carbon dioxide (SC-CO2) fracturing is a promising technology for unconventional energy development and carbon capture and storage. Experimental studies have shown that SC-CO2 fracturing can form complex fracture networks and reduce crack initiation pressure, which are different results from those when fracturing with aqueous fluids. The complex fracture networks that form from SC-CO2 fracturing may be the result of the strong seepage effect (i.e., low capillary and viscous forces). To understand the different injection behaviors induced by SC-CO2 and aqueous fluids in low-permeability rocks, this study develops a new two-phase steady-state model based on the pore-scale network method. Although other models consider the viscous force, our model implements the capillary and viscous forces to reproduce the seepage effect. Because of the capillary force, the flow model is nonlinear and solved by iteratively solving matrix equations until a conservation of volumetric flux is satisfied. Simulation results show that the capillary force in a two-phase flow is not negligible on pressure distribution in small pore spaces. This leads to discontinuous pressure drops. This study shows that the seepage effect of SC-CO2 is stronger than that of aqueous fluids.

Abstract

Supercritical carbon dioxide (SC-CO$_2$) fracturing is a promising technology for unconventional energy development and carbon capture and storage. Experimental studies have shown that SC-CO$_2$ fracturing can form complex fracture networks and reduce crack initiation pressure, which are different results from those when fracturing with aqueous fluids. The complex fracture networks that form from SC-CO$_2$ fracturing may be the result of the strong seepage effect (i.e., low capillary and viscous forces). To understand the different injection behaviors induced by SC-CO$_2$ and aqueous fluids in low-permeability rocks, this study develops a new two-phase steady-state model based on the pore-scale network method. Although other models consider the viscous force, our model implements the capillary and viscous forces to reproduce the seepage effect. Because of the capillary force, the flow model is nonlinear and solved by iteratively solving matrix equations until a conservation of volumetric flux is satisfied. Simulation results show that the capillary force in a two-phase flow is not negligible on pressure distribution in small pore spaces. This leads to discontinuous pressure drops. This study shows that the seepage effect of SC-CO$_2$ is stronger than that of aqueous fluids.

Keyword: Seepage effect; SC-CO$_2$ fracturing; Shale rock; Pore scale network model

We have read the comments of reviewers and editors. These comments have been constructively helpful to our article. In order to answer the comments of the reviewers, we divided the opinions into five major questions as follows:

Reviewers 1:

1. The fact that this model assumes steady-state conditions should be mentioned much earlier (including possibly the title) and more often.

We modified the title, body, conclusion of this papers as your suggested.

2. Therefore, there may very well be capillary resistance during at least some (if not all) of the period of most interest (i.e., injection). This should at least be discussed and considered in the manuscript.
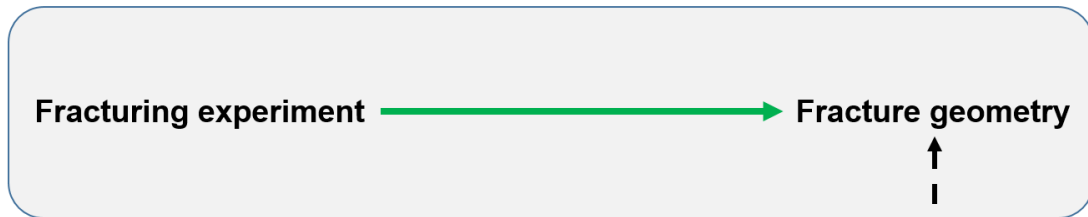
According reviewer's comment, we added contents to discuss this problem. Fracturing process contains a pressurization stage by injecting fracturing fluid into a borehole. If this period is long enough, the fracturing fluid is mixed well with the formation fluid (e.g., hydrocarbon) and the capillary resistance can be neglected. In the experiment from Zhang et al. (2017), the period of SC-CO_2 injection was over 7.0 minutes. We expect that this period could be long enough to mix between SC-CO2 and formation fluid in the view of the high diffusion coefficient of SC-CO_2. Even if the pressurization stage is not enough to make two different fluid mix well, the interfacial tension between SC-CO_2 and hydrocarbon is ultra-small. The interfacial tension between SC-CO_2 and hydrocarbon (gas) is less than 2mN/m (Li et al., 2017), while the interfacial tension between water and hydrocarbon (gas) is about 50mN/m. The capillary force between SC-CO_2 and hydrocarbon is much smaller than that between water and hydrocarbon. Thus, the effect of capillary force that occurs with SC-CO_2 is quite smaller than with water. Therefore, the capillary force between SC-CO_2 and formation fluid is neglected in our simulation.

3. While the authors drew good comparisons between their modeling outputs and analytical solutions, I wonder why more effort was not given to match their models with the experimental results they reference so often (Zhang et al., 2017). There may be a very plausible explanation for this. If so, it should be mentioned. If not, I believe a comparison to these data is warranted.
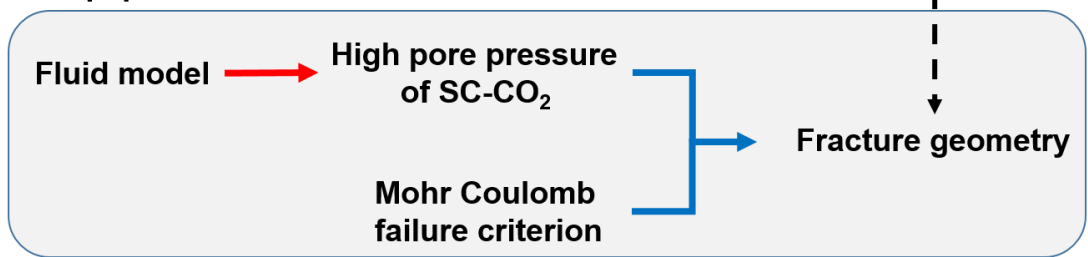
Their experiment (Zhang et al., 2017) were conducted to study different fracture patterns induced by water injection and SC-CO_2 injection. They indicated that the mechanism of forming complex fracture patterns was the effect of strong seepage effect. Thus, understanding of flow behaviors of SC-CO_2 is a challenge that must be overcome in the beginning, and is essential for reproducing complex fracture patterns. Therefore, this paper focuses on developing a new flow model considering the effects of viscous and capillary forces. Our results indicated that SC-CO_2 injection leads to relatively high pore pressure distributions in a wide area away from the well. Based on the Mohr-Coulomb failure criterion, the high pore pressure distributions likely results in shear failure in a wide area and should generate complex fracture

distributions. This finding is consistent with the experimental results. If the experiment could provide pore pressure distributions, we could compare pressure distributions with our simulation results. However, it is difficult to measure pore pressure distributions in an experiment, and their paper presented fracture geometries only. Thus, in this paper comparison with experimental results was in discussion only. We argued this in our manuscript. In our future work, we will develop a solid model and couple it with the current flow model to simulate fracture geometry and compare with the experiment result (Zhang et al., 2017) directly.
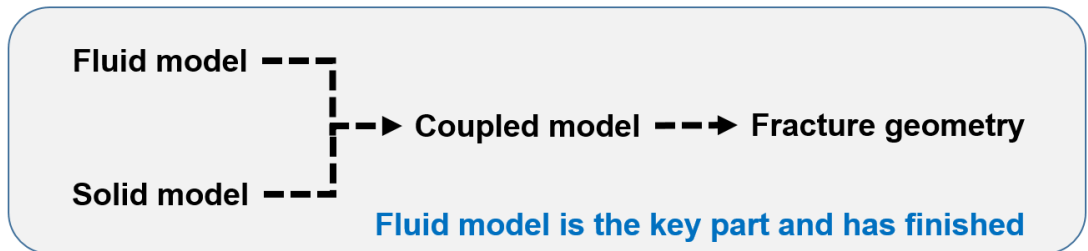
Zhang's experiment:

Fracturing experiment ⟶ **Fracture geometry**

Our paper:

Comparison

Fluid model ⟶ **High pore pressure of SC-CO$_2$**

Mohr Coulomb failure criterion

⟶ **Fracture geometry**

⟶ **Numerical simulation**   ⟶ **Inference**

Future work:

Fluid model ⇢

Solid model ⇢

⇢ **Coupled model** ⇢ **Fracture geometry**

Fluid model is the key part and has finished

4. Lastly, the writing of this manuscript needs a lot of work before it is publishable.

Thanks for suggestion about the writing. We amended the figures and sentences. In addition, the article was checked by native speaker.

Reviewers 2:

5. The abstract and Fig problems

According to the comment of reviewer, we delete the Fig.1 and add more details of the flow model in the abstract.

Reference

Li, N., Zhang, C.W., Ma, Q.L., Jiang, L.Y., Xu, Y.X., Chen, G.J., Sun, C.Y., Yang,
L.Y., 2017. Interfacial Tension Measurement and Calculation of (Carbon Dioxide
+ n-Alkane) Binary Mixtures. J. Chem. Eng. Data 62, 2861−2871.
https://doi.org/10.1021/acs.jced.7b00159

Zhang, X., Lu, Y., Tang, J., Zhou, Z., Liao, Y., 2017. Experimental study on fracture

initiation and propagation in shale using supercritical carbon dioxide fracturing.

Fuel 190, 370−378. https://doi.org/10.1016/j.fuel.2016.10.120

Estimating the Seepage Effect of SC-CO$_2$ and Water Fracturing with a Steady-state Flow Model: Consider Capillary and Viscous Forces in Pore Scale

Bailong Liu, Anna Suzuki, and Takatoshi Ito

Institute of Fluid Science, Tohoku University., Japan

Abstract

Supercritical carbon dioxide (SC-CO$_2$) fracturing is a promising technology for unconventional energy development and carbon capture and storage. Experimental studies have shown that SC-CO$_2$ fracturing can form complex fracture networks and reduce crack initiation pressure, which are different results from those when fracturing with aqueous fluids. The complex fracture networks that form from SC-CO$_2$ fracturing may be the result of the strong seepage effect (i.e., low capillary and viscous forces). To understand the different injection behaviors induced by SC-CO$_2$ and aqueous fluids in low-permeability rocks, this study develops a new two-phase steady-state model based on the pore-scale network method. Although other models consider the viscous force, our model implements the viscous and capillary forces to reproduce the seepage effect. Because of the capillary force, the flow model is nonlinear and solved by iteratively solving matrix equations until a conservation of volumetric flux is satisfied. Simulation results show that the capillary force in a two-phase flow is not negligible on pressure distribution in small pore spaces. This leads to discontinuous pressure drops. This study shows that the seepage effect of SC-CO$_2$ is stronger than that of aqueous fluids.

Keyword: Seepage effect; SC-CO$_2$ fracturing; Shale rock; Pore scale network

model

1. Introduction

Supercritical carbon dioxide (SC-CO$_2$) is a special fluid with a low viscosity (like gas) and high density (like liquid). Experimental studies have shown that SC-CO$_2$ has many potential advantages as a fracturing fluid. For instance, SC-CO$_2$ fracturing reduces initiation pressure by 50% or more (Zhang et al., 2017). Fractures induced by SC-CO$_2$ are irregular multiple cracks and easily form complex fracture networks, which are different from fractures induced by conventional aqueous fluids (Bennour et al., 2015; Ishida et al., 2016a; Zhang et al., 2017). These characteristics of SC-CO$_2$ fracturing yield positive effects on unconventional energy developments, including CO$_2$ sequestration and enhanced geothermal systems (Middleton et al., 2014; Reynolds et al., 2018).

Injected water can be an immiscible fluid in oil and gas reservoirs, whereas injected SC-CO$_2$ can be a miscible fluid. When comparing water injection and SC-CO$_2$ injection, two-phase flow should be considered. In addition, the different performances of SC-CO$_2$ fracturing from aqueous fluid fracturing are generally considered to derive from the strong seepage effects of SC-CO$_2$ (Ishida et al., 2016; Watanabe et al., 2017; Zhang et al., 2017). The seepage effect may be influenced by capillary and viscous forces in small pore spaces in a two-phase flow (Kantzas, Apostolos; Bryan Jonathan; Taheri, 2015). Strong seepage effects occur because of low viscous and low capillary forces, which may lead to increased percolation and increased pore pressure. Some studies have investigated pore pressure distribution

during fracturing, but their flow models have considered only the viscous force (Belytschko et al., 2000; Choo et al., 2016; Economides and Boney, 2000; Latham et al., 2011; Lecampion et al., 2017; Liu et al., 2018; Peng et al., 2017; Shi et al., 2017; Shimizu et al., 2011; Yan et al., 2016; Zhao et al., 2014). The capillary force cannot be ignored in low-permeability porous media such as shale rock when a two-phase flow occurs (Blunt, 2001; Higdon, 2013).

The pore-scale network model (PNM) has been developed to simulate flow in porous media (Valvatne, 2004), and some studies have simulated the multiphase flow in the pore scale using a PNM (Al-Gharbi and Blunt, 2005; Joekar-Niasar and Hassanizadeh, 2012; Wang et al., 2015). Because a PNM can consider small pore geometries, it is used to closely examine behaviors in the pore space.

In this study, a two-phase steady-state flow model is developed to investigate the seepage effects of SC-CO_2. The model integrates both capillary and viscous forces based on the PNM. We analyze the characteristics of the pressure field during fluid injection, which directly influence fracture geometries during fracturing. In addition, the difference between injection SC-CO_2 and injection water is discussed.

2. Model description

2.1 Pore-scale network models

The PNM is an effective model to represent flow in a porous medium through the pores and throats. In the fracturing process, injection fluid is pushed into formations, and the formation fluid is displaced. In general, three types of displacements can occur during fracturing: piston-like, pore-body filling, or snap-off (Valvatne, 2004).

The piston-like displacement refers to invasion into throats by fluid that were previously present in pores. In a pore-body filling displacement, fluid in pores is displaced by the fluid in throats. Snap-off displacement describes invasion by wetting fluid at the corner of a cross section when the pressure of the invasion fluid is lower than the threshold of the capillary pressure. The effect of snap-off displacement is known to be considerably smaller than the effects of the other two types of displacements in shale rocks (Al-Gharbi and Blunt, 2005). Thus, the current model considers only piston-like displacement and pore-body filling. In our network model, the triangular cross section was selected to consider the wetting phase flow (film flow) at the corners (Mogensen and Stenby, 1998; Nguyen et al., 2006).

Let us consider that there are two adjacent elements i and j. (Note that whether they are pores or throats is irrelevant.) The flow rate from element i to element j, q_{ij}, is given by:

$$q_{ij} = g_{ij}(P_i - P_j + P_{c,ij}) \#(1)$$

where g_{ij} is the flow conductivity between elements i and j. P_i and P_j are the pressures for elements i and j, respectively. $P_{c,ij}$ is the capillary force between elements i and j. The flow conductivity equations are given by (Hughes and Blunt, 2000):

$$g_{ij} = \int_0^L g(x) dx \#(2)$$

$$g(x) = 1/C(x), 0 \le x \le L \#(3)$$

where μ is the fluid viscosity, L is the length between elements i and j, and $C(x)$ is the fluid conductance per unit length and is determined by the fluid configuration in

their cross sections.

Two types of cross-section configurations (see Fig. 1(a)) can be generated when the injection fluid is different from the formation fluid: single-phase configuration (in a non-invaded element), C_{sp}; and two-phase configuration (in an invaded element), C_{tp}. The geometric parameters for calculating conductance and area are shown in Fig. 1(a).

For single-phase configuration, the fluid conductance per unit length, C_{sp}, is given by (Aker et al., 1998; Al-Gharbi, 2004):

$$C_{sp} = \frac{\pi \mu_w}{128} \left(R + (A_t/\pi)^{\frac{1}{2}} \right)^4 \quad \#(4)$$

where A_t is the cross-section area of the element and R is the inscribed radius of the cross section. The cross-section area of the element, A_t, is:

$$A_t = R^2 \sum_{i=1}^{n} \cot \alpha_i \quad \#(5)$$

where α_i is the half corner angle and n is the number of corners in the cross section.

For two-phase configuration, the wetting and non-wetting phases in the cross section should be considered. The fluid conductance per unit length for the two-phase configuration, C_{tp}, is described by:

$$C_{tp} = (C_{nw+}C_w)/C_{nw}C_w \quad \#(6)$$

where C_{nw} and C_w represent the conductance of the non-wetting phase and wetting phase fluids in the center and at the corner, respectively, which is given by (Aker et al., 1998; Al-Gharbi, 2004):

$$C_{nw} = \frac{\pi \mu_{nw}}{128} \left(R + (A_{nw}/\pi)^{\frac{1}{2}} \right)^4 \quad \#(7)$$

$$C_w = \mu_w \sum_{i=1}^{n} \left(\frac{A_{ci}(1 - \sin \alpha_i)\varphi_3}{\sin \alpha_i \, (1 - \varphi_3)(\varphi_2 + f\varphi_1)} \cdot \left(\frac{\varphi_2 \cos \theta - \varphi_1}{12} \right)^{\frac{1}{2}} \right)^2 \#(8)$$

The parameters φ_1, φ_2, and φ_3 depend on the half corner angle α and the contact

angle θ. The parameter f indicates the capacity of fluid crossing the fluid interface

(Piri and Blunt, 2005). In our model, the parameter f equals 1, which means that no

flow occurs on the fluid interface. The area of the formation fluid (wetting phase fluid)

at the corner, A_w, and injection fluid (non-wetting phase fluid) at the center, A_{nw}, are

calculated by:

$$A_w = \sum_{i=1}^{n} A_{ci} \#(9)$$

$$A_{ci} = r^2 \left(\cos \theta (\cot \alpha_i \cos \theta - \sin \theta) + \theta + \alpha_i - \frac{\pi}{2} \right) \#(10)$$

$$A_{nw} = A_t - A_w \#(11)$$

where r is the radius of the curvature of the interface.

For elements invaded by injection fluid (see Fig. 1(b)), the flow rate q_{ij} as given

in the following equation is divided into the flow rates of the wetting and non-wetting

phases as:

$$q_{ij} = q_{nw,ij} + q_{w,ij} \#(12)$$

The flow rate of each phase from element i to element j is given by:

$$q_{nw,ij} = q_{ij} \, C_{nw,i} / (C_{nw,i} + C_{w,i}) \#(13)$$

$$q_{nw,ij} = q_{ij} \, C_{w,i} / (C_{nw,i} + C_{w,i}) \#(14)$$

where $C_{w,i}$ and $C_{nw,i}$ represent the conductance of the non-wetting and wetting

phase fluids in element i, respectively.

The capillary force ($P_{c,ij}$) between element i and j is calculated using the

Young–Laplace equation:

$$P_{c,ij} = \frac{2\sigma \cos \theta}{r} \#(15)$$

where σ denotes interfacial tension between the two fluid phases.

Considering the small compressibility of SC-CO$_2$ (Vilarrasa et al., 2010), the conservation equation is applicable to SC-CO$_2$ flow. For either single- or two-phase flow, the conservation of the volume flux at element i can be described by:

$$\sum_{j=1}^{Z_i} q_{ij} = \sum_{j=1}^{Z_i} (q_{nw,ij} + q_{w,ij}) = 0 \#(16)$$

where Z_i is the number of elements connecting to element i. For instance, the pore i connects throats 1–3 in Fig. 2. The conservation of volume flux at pore i can be expressed as $q_{i2} + q_{i3} + q_{i1} = 0$.

Each pore connects more than one throat in our numerical model. Based on the flow rate of (1) − (16) and the topological structure of the network, the assembly equation can be formed as:

$$\begin{bmatrix} D_{11} & \cdots & D_{1j} \\ \vdots & \ddots & \vdots \\ D_{i1} & \cdots & D_{ij} \end{bmatrix} \begin{Bmatrix} P_1 \\ \vdots \\ P_i \end{Bmatrix} = \begin{Bmatrix} \sum_{j=1}^{Z_1} g_{1j} P_{c,1j} \\ \vdots \\ \sum_{j=1}^{Z_i} g_{ij} P_{c,ij} \end{Bmatrix} \#(17)$$

where D_{ij} is the conductance matrix. When $i = j$, $D_{ij} = \sum_{j=1}^{Z_i} g_{ij}$; otherwise, $D_{ij} = g_{ij}$.

2.2 Computational procedure

Based on the previous discussion, we derived the quasi-steady-state pressure distribution. To simulate fluid injection, a time variation of the fluid flow was calculated. We iterated to obtain the steady-state pressure distribution at each time

step Δt. The computational procedure, as shown in Fig. 3, is described as follows:

1) Based on the initial condition, the conductivity of each element is calculated by using (4) – (11). Then, the integral conductance matrix D_{ij} and force matrix are assembled.

2) As P_{outlet}^t and P_{inlet}^t are known, the pressure distribution is obtained from (17). Based on the pressure distribution, the total flow rate q_{ij}, the non-wetting phase flow rate $q_{nw,ij}$, and the wetting phase flow rate $q_{w,ij}$ can be solved though (1) and (12) – (14).

3) Calculate each phase fluid volume $V_{w,i}^{t+\Delta t}$ and $V_{nw,i}^{t+\Delta t}$ in element i at $t + \Delta t$ by using (18) – (19). Update the meniscus position and fluid configuration of each element based on each phase fluid volume. The purpose of choosing Δt is to ensure every meniscus will not cross one throat element in Δt. Then, the initial condition can be updated according to the configuration at $t + \Delta t$.

The volume of each of the wetting and non-wetting phases in element i can be expressed by:

$$V_{w,i}^{t+\Delta t} = V_{w,i}^t + \Delta t \times \sum_{j=1}^{z_i} q_{w,ij} \quad \#(18)$$

$$V_{nw,i}^{t+\Delta t} = V_{nw,i}^t + \Delta t \times \sum_{j=1}^{z_i} q_{nw,ij} \quad \#(19)$$

3. Simulation condition

We simulated seepage effects (capillary and viscous forces) for SC-CO$_2$ and water fracturing as previously examined in the SC-CO$_2$ and water fracturing experiment conducted by Zhang et al (Zhang et al., 2017).

3.1 Structure of PNM

Two pore network structures were used in the simulation cases. One structure, labeled Network A, was used to validate the flow model and investigate the difference between injecting SC-CO$_2$ and water, as shown in Fig. 4(a). Network A was used to represent two types of porous media: homogenous porous medium (PNM-homo) and heterogeneous porous medium (PNM-hetero). For PNM-homo, a constant average radius of pores and throats was set for a single simulation. To investigate the effects of different radii, the radii of pores and throats varied from 0.01 to 0.15 μm for each simulation. Thus, the sizes of the simulation models varied for different average radii of pores and throats, see Table 1. The lengths were normalized by the size of each simulation model. For PNM-hetero, the distributions of radii of throats and pores were generated based on the statistical data of sandstone (Bakke and Øren, 1997; Øren and Bakke, 2003, 2002), which is shown in Fig. 5. The other structure, Network B, was assumed to contain a pre-existing fracture (PNM-frac), which was to see pressure distribution around fracture. (see Fig. 4(b)). The size of Network B was consistent with the experimental sample of Zhang et al. (Zhang et al., 2017).

3.2 Fluid parameter and injection pressure

Four fluid systems and fluid viscosities, as listed in Tables 2 and 3, respectively, were used in the simulation and considered in the discussion. The formation fluid was gas or oil and the injection fluid was oil, water, or SC-CO$_2$. SC-CO$_2$ is miscible with hydrocarbons and has a high diffusion coefficient. In the fracturing process, a pressurization stage occurs before crack initiation. At this pressurization stage, SC-CO$_2$ can fully dissolve with the formation fluid at the interface area. The interface between SC-CO$_2$ and hydrocarbon (gas or oil) disappears and the capillary force

decreases to zero. Before SC-CO$_2$ dissolves sufficiently into a formation fluid, the interfacial tension between SC-CO$_2$ and hydrocarbon is very small, approximately 2 mN/m (Li et al., 2017). The interfacial tension between water and hydrocarbon is approximately 50 mN/m. Thus, our simulation assumed that the capillary force between SC-CO$_2$ and the formation fluids (oil or gas) was negligible.

The inlet and outlet pressure values were derived from the fracturing experimental conditions of Zhang et al. (Zhang et al., 2017). In their experiment, the injection pressure was approximately 5 MPa after fracture initiation. Considering the pressure loss in tube, 4 MPa was used as the inlet pressure. However, 8 MPa was also set as the inlet pressure to ensure that the inlet pressure was higher than the threshold of the capillary force for different radii.

4. Validation

A validation of the flow model was conducted by comparing the analytical solutions in different flow situations: a) single-phase flow (the injection and formation fluids were the same); b) two-phase flow without considering the capillary force (*Pc*). The analytical solutions were based on the Buckley-Leverett theory (Buckley and Leverett, 1942; Idowu and Blunt, 2010). These solutions and the numerical results obtained from the flow model are plotted in Fig. 6. The numerical results of the single- and two-phase flows without capillary force were confirmed to be in good agreement with the analytical results derived from the homogeneous porous medium.

5. Simulation and results

To investigate the seepage effects of SC-CO$_2$ injection, five simulations were

conducted. Both capillary and viscous forces were integrated into the PNM to simulate the pressure field for a two-phase flow. The different injection conditions are listed in Table 4.

5.1 Effects of capillary force

The effects of capillary force on two-phase flow are presented in Fig. 7. The PNM-homo was used to simulate the effect of the capillary force. The constant pore-throat radius was set to $0.1 \, \mu m$. The results yielded snapshots of the pressure distributions derived from water injection with and without capillary force. Water was injected from the inlet (normalized length = 0). The case without Pc only considered the effect of viscous force, whereas that with Pc considered the effects of both viscous and capillary forces. When the capillary force was considered, a discontinuous pressure drop (DPD) occurred. The capillary force posed an extra resistant force to block the invasion of water. This resistant force derived from the capillary force could cause a DPD in the two-phase flow.

5.2 Effects of injection time

Water or SC-CO$_2$ injections were simulated in a homogeneous porous medium using PNM-homo. The constant average pore-throat radius was $0.1 \, \mu m$. The time variation of the pressure field is shown in Fig. 8. Water or SC-CO$_2$ was injected from the inlet (normalized length = 0), and the pressure field of the water injection, as shown in Fig.8(a), experienced a DPD that was caused by the capillary force. The injection fluid (water) was immiscible with the formation fluid (oil). When they met during injection, the capillary force was generated at the interface between water and

oil. With continuous injection, DPD continuously affected the pressure field. The positions of the DPD moved to the outlet side because of changes in the interfacial position between water and oil.

By contrast, the pressure field of the SC-CO$_2$ injection experienced no DPD, as shown in Fig. 8(b). Because SC-CO$_2$ and oil are miscible, no interface existed between them. In other words, no capillary force occurred between SC-CO$_2$ and oil, which means that no DPD occurred. Fig. 8(b) also shows that the slope of the pressure curve in the area displaced by SC-CO$_2$ (inlet side) was flatter than the area occupied by oil (outlet side). This was caused by both low viscous and low capillary forces of SC-CO$_2$, (i.e., the seepage effect). Because the injected SC-CO$_2$ penetrated into pores easily given a small pressure drop, pressure propagation was advanced with a value that approximated the injection pressure. The change points of slopes could be considered the interfacial positions between SC-CO$_2$ and oil. The interfacial position between SC-CO$_2$ and oil was ahead of that between water and oil. This indicated that the seepage effect of SC-CO$_2$ promoted the advancement of the interfacial front.

5.3 Effects of pore and throat radii

The influence of different pore-throat radii on the pressure field was investigated when considering the capillary and viscous forces using PNM-homo. The average pore-throat radii and corresponding permeability are listed in Table 5. These parameters were derived from the experiments with shale rocks (Lu et al., 2018). The sizes of simulation models for each pore radius are listed in Table 1.

Fig. 9(a) and (b) show the differences in the pressure fields between water and SC-CO$_2$ injections, respectively, in a homogeneous porous medium. Fig. 9(a) reveals

that the values of DPDs varied for the different average pore-throat radii. The DPD was influenced by the geometries of pore and throat. Because the DPD occurred as a result of the capillary force, the simulation results indicate that the capillary force could not be neglected due to the low permeability of rock when the injection fluid (water) was immiscible with the formation fluid (oil).

By contrast, with the SC-CO$_2$ injection, no DPD occurred, as shown in Fig. 9(b). The pressure field for the SC-CO$_2$ injection was controlled solely by the viscous force. Because of the low viscosity of SC-CO$_2$, the pressure distributions for different average pore-throat radii in small distances were nearly the same.

5.4 Heterogeneous porous medium

Rock for the most part is a heterogeneous porous media. Thus, investigating the pressure performances of water and SC-CO$_2$ injections in heterogeneous porous media is necessary. In our study, even the radius distributions were random, where the total average radius of the pore-throat for all pores and throats was $0.02\,\mu m$. The corresponding sample sizes are listed in Table 1.

A DPD occurred with water injection (Fig. 10(a)), but no DPD occurred with SC-CO$_2$ injection (Fig. 10(b)) in the heterogeneous porous medium. This indicated that the capillary and viscous forces affected the pressure fields in heterogeneous rocks. The results reveal that DPD clearly occurred when the injected fluid (water) was immiscible with the formation fluid (oil). For SC-CO$_2$, the property of miscibility with hydrocarbon produces a strong seepage effect.

5.5 Well injection with pre-existing fracture

Similar conditions as those in the experiment of Zhang et al. (Zhang et al., 2017)

were simulated using the PNM-frac. The formation fluid was assumed to be gas, which was intended to represent shale gas rock (hydrocarbon wet). The average pore-throat radius was set to 0.01 μm. The simulation results of pressure distributions for water and SC-CO_2 injections are presented in Fig. 11. The simulation results revealed that the DPD derived from the capillary force between water and gas blocked the spread of pressure (see Fig. 11(a)). However, in the case of SC-CO_2 injection, pressure spread easily without blocks because of the absence of capillary forces, as shown in Fig. 11(b). This indicated that the capillary force could cut off the pressure when the injection pressure was insufficient to overcome the threshold of the capillary force. It should be noted that the pore pressure in non-invaded elements in this model was set to 0 MPa.

5.6 Discussion of capillary force effect on the fracture geometry

In general, fracturing with water leads to tensile failure, which in turn generates fractures, and these fractures extend directly in the direction of the main stress. The simulation results for water injection suggested that the pressure spread was blocked by the capillary and viscous forces. However, the effect of capillary force on SC-CO_2 injection was negligible, and the viscous force for SC-CO_2 injection was lower than for water injection. The pressure could penetrate into the pore and throat around any pre-existing fracture. This can cause the pore pressure to increase considerably as compared with using water as injection fluid. When the pore pressure increased, the effective stress decreased. If we consider the Mohr-Coulomb failure criterion, shear failure events occur easily with a small effective stress (i.e., high pore pressure), as

shown in Fig.12(a). Therefore, increased pore pressure due to SC-CO_2 injection likely initiates shear failure cracks. Typically, a crack caused by shear failure is not parallel to a fracture caused by tensile failure (Labuz and Zang, 2012; Patton, 1966). Fracturing due to SC-CO_2 injection may lead to more branched and high tortuous fractures as well as rough fracture surfaces. Thus, the facture geometry derived from SC-CO_2 injection should be more complex than water injection because of shear failure cracks (see Fig. 12(b)). These inferred behaviors are consistent with the experimental results of Zhang et al., who showed that the fracture geometry of SC-CO_2 was more complex than water fracturing.

In fact, this paper is based on a flow model to study different pressure performance when injecting water and SC-CO_2. On this basis, combined with the Mohr-Coulomb failure criterion, it is concluded that SC-CO_2 fracturing should induce complex fracture. But this conclusion is not directly obtained through simulation. Therefore, in the following work, we will develop a solid model and couple it with the flow model to verify the aforementioned results that the fracture pattern induced by SC-CO_2 fracturing is complex fracture networks.

6. Conclusion

A two-phase steady-state flow model considering the effects of capillary and viscous forces was developed to investigate differences between aqueous and SC-CO_2 injections. The results of this study can be summarized as follows.

With respect to aqueous fluid injection, the pressure field was influenced by the capillary force because of immiscibility. The capillary force produced DPDs at the

interfacial points. The effects of capillary force, on aqueous fluid, were significant with respect to low-permeability reservoirs. However, miscible fluid, such as SC-CO$_2$ reduced the effect of the capillary force and prevented DPD. Miscibility with hydrocarbon and the low viscosity of SC-CO$_2$ led to a strong seepage effect. The strong seepage effect of SC-CO$_2$ increased pore pressure ~~in wide areas~~ and induced shear fractures. This typically leads to the formation of complex fracture networks.

Acknowledgement

Author contributions

B. Liu planed and conducted the study. A. Suzuki contributed the design of the study. T. Ito contributed on the examination of the paper structure. All authors participated in the discussion and interpretation of results, as well as the writing of the manuscript.

Funding

Nomenclature

g conductance, $m^3/(\text{Pa.s})$;

L length of an element, m;

n number of corners;

z number of elements connecting to element i;

α_i half corner angle at corner i;

P pressure, Pa;

P_c capillary pressure, Pa;

q volumetric flow rate, m^3/s;

r the curvature radius of corner interface, m;

R inscribed radius of a cross-section, m;

Δt time-step size, s;

θ contact angle, radian;

σ interfacial tension between two fluid phases, N/m;

μ fluid viscosity, Pa · s;

V fluid volume in an element, m^3;

nw non-wetting phase;

w wetting phase;

C conductance of fluid in cross section, Pa. s/m^4

S_H, S_h Maximum principal stress and minimum principal stress

Reference

Aker, E., JØrgen MÅlØy, K., Hansen, A., Batrouni, G.G., 1998. A two-dimensional

network simulator for two-phase flow in porous media. Transp. Porous Media 32,

163–186. https://doi.org/10.1023/A:1006510106194

Al-Gharbi, M.S., 2004. Dynamic pore-scale modelling of two-phase flow. Imperial

College London.

Al-Gharbi, M.S., Blunt, M.J., 2005. Dynamic network modeling of two-phase

drainage in porous media. Phys. Rev. E - Stat. Nonlinear, Soft Matter Phys. 71,

1–16. https://doi.org/10.1103/PhysRevE.71.016308

Bakke, S., Øren, P.-E., 1997. 3-D Pore-scale modelling of sandstones and flow

simulations in the pore networks. SPE J. https://doi.org/10.2118/35479-PA

Belytschko, T., Organ, D., Gerlach, C., 2000. Element-free galerkin methods for

dynamic fracture in concrete. Comput. Methods Appl. Mech. Eng. 187, 385–399.

https://doi.org/10.1016/S0045-7825(00)80002-X

Bennour, Z., Ishida, T., Nagaya, Y., Chen, Y., Nara, Y., Chen, Q., Sekine, K., Nagano,

Y., 2015. Crack extension in hydraulic fracturing of shale cores using viscous oil,

water, and liquid carbon dioxide. Rock Mech. Rock Eng. 48, 1463–1473.

https://doi.org/10.1007/s00603-015-0774-2

Blunt, M.J., 2001. Flow in porous media - pore-network models and multiphase flow.

Curr. Opin. Colloid Interface Sci.

https://doi.org/10.1016/S1359-0294(01)00084-X

Buckley, S.E., Leverett, M.C., 1942. Mechanism of fluid displacement in sands. Trans.

AIME. https://doi.org/10.2118/942107-G

Choo, L.Q., Zhao, Z., Chen, H., Tian, Q., 2016. Hydraulic fracturing modeling using

the discontinuous deformation analysis (DDA) method. Comput. Geotech. 76,

12–22. https://doi.org/10.1016/j.compgeo.2016.02.011

Economides, M.J., Boney, C., 2000. Reservoir stimulation. Reserv. Stimul.

https://doi.org/10.1017/CBO9781107415324.004

Higdon, J.J.L., 2013. Multiphase flow in porous media. J. Fluid Mech.

https://doi.org/10.1017/jfm.2013.296

Hughes, R.G., Blunt, M.J., 2000. Pore scale modeling of rate effects in imbibition.

Transp. Porous Media 40, 295–322. https://doi.org/10.1023/A:1006629019153

Idowu, N.A., Blunt, M.J., 2010. Pore-scale modelling of rate effects in waterflooding.

Transp. Porous Media 83, 151–169. https://doi.org/10.1007/s11242-009-9468-0

Ishida, T., Chen, Y., Bennour, Z., Yamashita, H., Inui, S., Nagaya, Y., Naoi, M., Chen,

Q., Nakayama, Y., Nagano, Y., 2016a. Features of CO_2 fracturing deduced from

acoustic emission and microscopy in laboratory experiments. J. Geophys. Res.

Solid Earth 121, 8080–8098. https://doi.org/10.1002/2016JB013365

Ishida, T., Chen, Y., Bennour, Z., Yamashita, H., Inui, S., Nagaya, Y., Naoi, M., Chen,

Q., Nakayama, Y., Nagano, Y., 2016b. Features of CO_2 fracturing deduced from

acoustic emission and microscopy in laboratory experiments. J. Geophys. Res.

Solid Earth. https://doi.org/10.1002/2016JB013365

Joekar-Niasar, V., Hassanizadeh, S.M., 2012. Analysis of fundamentals of two-phase

flow in porous media using dynamic pore-network models: A review. Crit. Rev.

Environ. Sci. Technol. 42, 1895–1976.

https://doi.org/10.1080/10643389.2011.574101

Kantzas, Apostolos; Bryan Jonathan; Taheri, S., 2015. Fundamentals of fluid flow in

porous media 336.

Labuz, J.F., Zang, A., 2012. Mohr-Coulomb failure criterion. Rock Mech. Rock Eng.

https://doi.org/10.1007/s00603-012-0281-7

Latham, J., Guo, L., Wang, X., Xiang, J., 2011. Modelling the evolution of fractures

using a combined FEM-DEM numerical method. Harmon. Rock Eng. Environ. 449–454. https://doi.org/10.1201/b11646-77

Lecampion, B., Bunger, A., Zhang, X., 2017. Numerical methods for hydraulic fracture propagation: A review of recent trends. J. Nat. Gas Sci. Eng. https://doi.org/10.1016/j.jngse.2017.10.012

Liu, Q., Sun, L., Liu, P., Chen, L., 2018. Modeling simultaneous multiple fracturing using the combined finite-discrete element method. Geofluids 2018. https://doi.org/10.1155/2018/4252904

Lu, S., Li, J., Zhang, P., Xue, H., Wang, G., Zhang, J., Liu, H., Li, Z., 2018. Classification of microscopic pore-throats and the grading evaluation on shale oil reservoirs. Pet. Explor. Dev. 45, 452–460. https://doi.org/10.1016/S1876-3804(18)30050-8

Middleton, R., Viswanathan, H., Currier, R., Gupta, R., 2014. CO_2 as a fracturing fluid: Potential for commercial-scale shale gas production and CO_2 sequestration. Energy Procedia 63, 7780–7784. https://doi.org/10.1016/j.egypro.2014.11.812

Mogensen, K., Stenby, E.H., 1998. A dynamic two-phase pore-scale model of imbibition. Transp. Porous Media 32, 299–327. https://doi.org/10.1023/a:1006578721129

Nguyen, V.H., Sheppard, A.P., Knackstedt, M.A., Val Pinczewski, W., 2006. The effect of displacement rate on imbibition relative permeability and residual saturation. J. Pet. Sci. Eng. 52, 54–70. https://doi.org/10.1016/j.petrol.2006.03.020

Øren, P.E., Bakke, S., 2003. Reconstruction of Berea sandstone and pore-scale

modelling of wettability effects. J. Pet. Sci. Eng.

https://doi.org/10.1016/S0920-4105(03)00062-7

Øren, P.E., Bakke, S., 2002. Process based reconstruction of sandstones and

prediction of transport properties. Transp. Porous Media.

https://doi.org/10.1023/A:1015031122338

Patton, F.D., 1966. Multiple modes of shear failure in rock. 1st Int. Congr. Rock

Mech.

Peng, P., Ju, Y., Wang, Y., Wang, S., Gao, F., 2017. Numerical analysis of the effect

of natural microcracks on the supercritical CO_2 fracturing crack network of shale rock

based on bonded particle models. Int. J. Numer. Anal. Methods Geomech.

https://doi.org/10.1002/nag.2712

Piri, M., Blunt, M.J., 2005. Three-dimensional mixed-wet random pore-scale network

modeling of two- And three-phase flow in porous media. I. Model description.

Phys. Rev. E - Stat. Nonlinear, Soft Matter Phys. 71, 1–30.

https://doi.org/10.1103/PhysRevE.71.026301

Reynolds, C.A., Blunt, M.J., Krevor, S., 2018. Multiphase Flow Characteristics of

Heterogeneous Rocks From CO_2 Storage Reservoirs in the United Kingdom.

Water Resour. Res. https://doi.org/10.1002/2017WR021651

Shi, F., Wang, X.L., Liu, C., Liu, H., Wu, H.A., 2017. An XFEM-based method with

reduction technique for modeling hydraulic fracture propagation in formations

containing frictional natural fractures. Eng. Fract. Mech. 173, 64–90.

Shimizu, H., Murata, S., Ishida, T., 2011. The distinct element analysis for hydraulic

fracturing in hard rock considering fluid viscosity and particle size distribution.

Int. J. Rock Mech. Min. Sci. 48, 712–727.

https://doi.org/10.1016/j.ijrmms.2011.04.013

Valvatne, H., 2004. Predictive pore-scale modelling of multiphase flow 146.

Vilarrasa, V., Bolster, D., Dentz, M., Olivella, S., Carrera, J., 2010. Effects of CO_2

compressibility on CO_2 storage in deep saline aquifers. Transp. Porous Media.

https://doi.org/10.1007/s11242-010-9582-z

Wang, S., Feng, Q., Dong, Y., Han, X., Wang, S., 2015. A dynamic pore-scale

network model for two-phase imbibition. J. Nat. Gas Sci. Eng. 26, 118–129.

https://doi.org/10.1016/j.jngse.2015.06.005

Watanabe, N., Egawa, M., Sakaguchi, K., Ishibashi, T., Tsuchiya, N., 2017. Hydraulic

fracturing and permeability enhancement in granite from subcritical/brittle to

supercritical/ductile conditions. Geophys. Res. Lett. 44, 5468–5475.

https://doi.org/10.1002/2017GL073898

Yan, C., Zheng, H., Sun, G., Ge, X., 2016. Combined finite-discrete element method

for simulation of hydraulic fracturing. Rock Mech. Rock Eng. 49, 1389–1410.

https://doi.org/10.1007/s00603-015-0816-9

Zhang, X., Lu, Y., Tang, J., Zhou, Z., Liao, Y., 2017. Experimental study on fracture

initiation and propagation in shale using supercritical carbon dioxide fracturing.

Fuel 190, 370–378. https://doi.org/10.1016/j.fuel.2016.10.120

Zhao, Q., Lisjak, A., Mahabadi, O., Liu, Q., Grasselli, G., 2014. Numerical simulation

of hydraulic fracturing and associated microseismicity using finite-discrete

element method. J. Rock Mech. Geotech. Eng. 6, 574–581.

https://doi.org/10.1016/j.jrmge.2014.10.003

Estimating the Seepage Effect of SC-CO$_2$ and Water Fracturing with a

Steady-state Flow Model: Consider Capillary and Viscous Forces in Pore Scale

Bailong Liu, Anna Suzuki, and Takatoshi Ito

Institute of Fluid Science, Tohoku University., Japan

Abstract

Supercritical carbon dioxide (SC-CO$_2$) fracturing is a promising technology for unconventional energy development and carbon capture and storage. Experimental studies have shown that SC-CO$_2$ fracturing can form complex fracture networks and reduce crack initiation pressure, which are different results from those when fracturing with aqueous fluids. The complex fracture networks that form from SC-CO$_2$ fracturing may be the result of the strong seepage effect (i.e., low capillary and viscous forces). To understand the different injection behaviors induced by SC-CO$_2$ and aqueous fluids in low-permeability rocks, this study develops a new two-phase steady-state model based on the pore-scale network method. Although other models consider the viscous force, our model implements the capillary and viscous forces to reproduce the seepage effect. Because of the capillary force, the flow model is nonlinear and solved by iteratively solving matrix equations until a conservation of volumetric flux is satisfied. Simulation results show that the capillary force in a two-phase flow is not negligible on pressure distribution in small pore spaces. This leads to discontinuous pressure drops. This study shows that the seepage effect of SC-CO$_2$ is stronger than that of aqueous fluids.

Keyword: Seepage effect; SC-CO$_2$ fracturing; Shale rock; Pore scale network

model

1. Introduction

Supercritical carbon dioxide (SC-CO$_2$) is a special fluid with a low viscosity (like gas) and high density (like liquid). Experimental studies have shown that SC-CO$_2$ has many potential advantages as a fracturing fluid. For instance, SC-CO$_2$ fracturing reduces initiation pressure by 50% or more (Zhang et al., 2017). Fractures induced by SC-CO$_2$ are irregular multiple cracks and easily form complex fracture networks, which are different from fractures induced by conventional aqueous fluids (Bennour et al., 2015; Ishida et al., 2016a; Zhang et al., 2017). These characteristics of SC-CO$_2$ fracturing yield positive effects on unconventional energy developments, including CO$_2$ sequestration and enhanced geothermal systems (Middleton et al., 2014; Reynolds et al., 2018).

Injected water can be an immiscible fluid in oil and gas reservoirs, whereas injected SC-CO$_2$ can be a miscible fluid. When comparing water injection and SC-CO$_2$ injection, two-phase flow should be considered. In addition, the different performances of SC-CO$_2$ fracturing from aqueous fluid fracturing are generally considered to derive from the strong seepage effects of SC-CO$_2$ (Ishida et al., 2016; Watanabe et al., 2017; Zhang et al., 2017). The seepage effect may be influenced by capillary and viscous forces in small pore spaces in a two-phase flow (Kantzas, Apostolos; Bryan Jonathan; Taheri, 2015). Strong seepage effects occur because of low viscous and low capillary forces, which often lead to increased percolation and increased pore pressure. Some studies have investigated pore pressure distribution

during fracturing, but their flow models have considered only the viscous force (Belytschko et al., 2000; Choo et al., 2016; Economides and Boney, 2000; Latham et al., 2011; Lecampion et al., 2017; Liu et al., 2018; Peng et al., 2017; Shi et al., 2017; Shimizu et al., 2011; Yan et al., 2016; Zhao et al., 2014). The capillary force cannot be ignored in low-permeability porous media such as shale rock when a two-phase flow occurs (Blunt, 2001; Higdon, 2013).

The pore-scale network model (PNM) has been developed to simulate flow in porous media (Valvatne, 2004), and some studies have simulated the multiphase flow in the pore scale using a PNM (Al-Gharbi and Blunt, 2005; Joekar-Niasar and Hassanizadeh, 2012; Wang et al., 2015). Because a PNM can consider small pore geometries, it is used to closely examine behaviors in the pore space.

In this study, a two-phase steady-state flow model is developed to investigate the seepage effects of SC-CO$_2$. The model integrates both capillary and viscous forces based on the PNM. We analyze the characteristics of the pressure field during fluid injection, which directly influence fracture geometries during fracturing. In addition, the difference between injection SC-CO$_2$ and injection water is discussed.

2. Model description

2.1 Pore-scale network models

The PNM is an effective model to represent flow in a porous medium through the pores and throats. In the fracturing process, injection fluid is pushed into formations, and the formation fluid is displaced. In general, three types of displacements can occur during fracturing: piston-like, pore-body filling, or snap-off (Valvatne, 2004).

The piston-like displacement refers to invasion into throats by fluid that were previously present in pores. In a pore-body filling displacement, fluid in pores is displaced by the fluid in throats. Snap-off displacement describes invasion by wetting fluid at the corner of a cross section when the pressure of the invasion fluid is lower than the threshold of the capillary pressure. The effect of snap-off displacement is known to be considerably smaller than the effects of the other two types of displacements in shale rocks (Al-Gharbi and Blunt, 2005). Thus, the current model considers only piston-like displacement and pore-body filling. In our network model, the triangular cross section was selected to consider the wetting phase flow (film flow) at the corners (Mogensen and Stenby, 1998; Nguyen et al., 2006).

Let us consider that there are two adjacent elements i and j. (Note that whether they are pores or throats is irrelevant.) The flow rate from element i to element j, q_{ij}, is given by:

$$q_{ij} = g_{ij}\left(P_i - P_j + P_{c,ij}\right) \#(1)$$

where g_{ij} is the flow conductivity between elements i and j. P_i and P_j are the pressures for elements i and j, respectively. $P_{c,ij}$ is the capillary force between elements i and j. The flow conductivity equations are given by (Hughes and Blunt, 2000):

$$g_{ij} = \int_0^L g(x)dx \#(2)$$

$$g(x) = 1/C(x), 0 \leq x \leq L \#(3)$$

where μ is the fluid viscosity, L is the length between elements i and j, and $C(x)$ is the fluid conductance per unit length and is determined by the fluid configuration in

their cross sections.

Two types of cross-section configurations (see Fig. 1(a)) can be generated when the injection fluid is different from the formation fluid: single-phase configuration (in a non-invaded element), C_{sp}; and two-phase configuration (in an invaded element), C_{tp}. The geometric parameters for calculating conductance and area are shown in Fig. 1(a).

For single-phase configuration, the fluid conductance per unit length, C_{sp}, is given by (Aker et al., 1998; Al-Gharbi, 2004):

$$C_{sp} = \frac{\pi \mu_w}{128} \left(R + (A_t/\pi)^{\frac{1}{2}} \right)^4 \#(4)$$

where A_t is the cross-section area of the element and R is the inscribed radius of the cross section. The cross-section area of the element, A_t, is:

$$A_t = R^2 \sum_{i=1}^{n} \cot \alpha_i \#(5)$$

where α_i is the half corner angle and n is the number of corners in the cross section.

For two-phase configuration, the wetting and non-wetting phases in the cross section should be considered. The fluid conductance per unit length for the two-phase configuration, C_{tp}, is described by:

$$C_{tp} = (C_{nw+}C_w)/C_{nw}C_w \#(6)$$

where C_{nw} and C_w represent the conductance of the non-wetting phase and wetting phase fluids in the center and at the corner, respectively, which is given by (Aker et al., 1998; Al-Gharbi, 2004):

$$C_{nw} = \frac{\pi \mu_{nw}}{128} \left(R + (A_{nw}/\pi)^{\frac{1}{2}} \right)^4 \#(7)$$

$$C_w = \mu_w \sum_{i=1}^{n} \left(\frac{A_{ci}(1 - \sin \alpha_i)\varphi_3}{\sin \alpha_i \, (1 - \varphi_3)(\varphi_2 + f\varphi_1)} \cdot \left(\frac{\varphi_2 \cos \theta - \varphi_1}{12} \right)^{\frac{1}{2}} \right)^2 \quad \#(8)$$

The parameters φ_1, $\varphi_{2,}$ and φ_3 depend on the half corner angle α and the contact

angle θ. The parameter f indicates the capacity of fluid crossing the fluid interface

(Piri and Blunt, 2005). In our model, the parameter f equals 1, which means that no

flow occurs on the fluid interface. The area of the formation fluid (wetting phase fluid)

at the corner, A_w, and injection fluid (non-wetting phase fluid) at the center, A_{nw}, are

calculated by:

$$A_w = \sum_{i=1}^{n} A_{ci} \quad \#(9)$$

$$A_{ci} = r^2 \left(\cos \theta (\cot \alpha_i \cos \theta - \sin \theta) + \theta + \alpha_i - \frac{\pi}{2} \right) \#(10)$$

$$A_{nw} = A_t - A_w \#(11)$$

where r is the radius of the curvature of the interface.

For elements invaded by injection fluid (see Fig. 1(b)), the flow rate q_{ij} as given

in the following equation is divided into the flow rates of the wetting and non-wetting

phases as:

$$q_{ij} = q_{nw,ij} + q_{w,ij} \#(12)$$

The flow rate of each phase from element i to element j is given by:

$$q_{nw,ij} = q_{ij} \, C_{nw,i}/(C_{nw,i} + C_{w,i}) \#(13)$$

$$q_{nw,ij} = q_{ij} \, C_{w,i}/(C_{nw,i} + C_{w,i}) \#(14)$$

where $C_{w,i}$ and $C_{nw,i}$ represent the conductance of the non-wetting and wetting

phase fluids in element i, respectively.

The capillary force ($P_{c,ij}$) between element i and j is calculated using the

Young–Laplace equation:

$$P_{c,ij} = \frac{2\sigma\cos\theta}{r} \#(15)$$

where σ denotes interfacial tension between the two fluid phases.

Considering the small compressibility of SC-CO$_2$ (Vilarrasa et al., 2010), the conservation equation is applicable to SC-CO$_2$ flow. For either single- or two-phase flow, the conservation of the volume flux at element i can be described by:

$$\sum_{j=1}^{Z_i} q_{ij} = \sum_{j=1}^{Z_i} (q_{nw,ij} + q_{w,ij}) = 0 \#(16)$$

where Z_i is the number of elements connecting to element i. For instance, the pore i connects throats 1–3 in Fig. 2. The conservation of volume flux at pore i can be expressed as $q_{i2} + q_{i3} + q_{i1} = 0$.

Each pore connects more than one throat in our numerical model. Based on the flow rate of (1) – (16) and the topological structure of the network, the assembly equation can be formed as:

$$\begin{bmatrix} D_{11} & \cdots & D_{1j} \\ \vdots & \ddots & \vdots \\ D_{i1} & \cdots & D_{ij} \end{bmatrix} \begin{Bmatrix} P_1 \\ \vdots \\ P_i \end{Bmatrix} = \begin{Bmatrix} \sum_{j=1}^{Z_1} g_{1j} P_{c,1j} \\ \vdots \\ \sum_{j=1}^{Z_i} g_{ij} P_{c,ij} \end{Bmatrix} \#(17)$$

where D_{ij} is the conductance matrix. When $i = j$, $D_{ij} = \sum_{j=1}^{Z_i} g_{ij}$; otherwise, $D_{ij} = g_{ij}$.

2.2 Computational procedure

Based on the previous discussion, we derived the quasi-steady-state pressure distribution. To simulate fluid injection, a time variation of the fluid flow was calculated. We iterated to obtain the steady-state pressure distribution at each time

step Δt. The computational procedure, as shown in Fig. 3, is described as follows:

1) Based on the initial condition, the conductivity of each element is calculated by using (4) – (11). Then, the integral conductance matrix D_{ij} and force matrix are assembled.

2) As P_{outlet}^t and P_{inlet}^t are known, the pressure distribution is obtained from (17). Based on the pressure distribution, the total flow rate q_{ij}, the non-wetting phase flow rate $q_{nw,ij}$, and the wetting phase flow rate $q_{w,ij}$ can be solved though (1) and (12) – (14).

3) Calculate each phase fluid volume $V_{w,i}^{t+\Delta t}$ and $V_{nw,i}^{t+\Delta t}$ in element i at $t + \Delta t$ by using (18) – (19). Update the meniscus position and fluid configuration of each element based on each phase fluid volume. The purpose of choosing Δt is to ensure every meniscus will not cross one throat element in Δt. Then, the initial condition can be updated according to the configuration at $t + \Delta t$.

The volume of each of the wetting and non-wetting phases in element i can be expressed by:

$$V_{w,i}^{t+\Delta t} = V_{w,i}^t + \Delta t \times \sum_{j=1}^{z_i} q_{w,ij} \#(18)$$

$$V_{nw,i}^{t+\Delta t} = V_{nw,i}^t + \Delta t \times \sum_{j=1}^{z_i} q_{nw,ij} \#(19)$$

3. Simulation condition

We simulated seepage effects (capillary and viscous forces) for SC-CO$_2$ and water fracturing as previously examined in the SC-CO$_2$ and water fracturing experiment conducted by Zhang et al (Zhang et al., 2017).

3.1 Structure of PNM

Two pore network structures were used in the simulation cases. One structure, labeled Network A, was used to validate the flow model and investigate the difference between injecting SC-CO$_2$ and water, as shown in Fig. 4(a). Network A was used to represent two types of porous media: homogenous porous medium (PNM-homo) and heterogeneous porous medium (PNM-hetero). For PNM-homo, a constant average radius of pores and throats was set for a single simulation. To investigate the effects of different radii, the radii of pores and throats varied from 0.01 to 0.15 μm for each simulation. Thus, the sizes of the simulation models varied for different average radii of pores and throats, see Table 1. The lengths were normalized by the size of each simulation model. For PNM-hetero, the distributions of radii of throats and pores were generated based on the statistical data of sandstone (Bakke and Øren, 1997; Øren and Bakke, 2003, 2002), which is shown in Fig. 5. The other structure, Network B, was assumed to contain a pre-existing fracture (PNM-frac), which was to see pressure distribution around fracture. (see Fig. 4(b)). The size of Network B was consistent with the experimental sample of Zhang et al. (Zhang et al., 2017).

3.2 Fluid parameter and injection pressure

Four fluid systems and fluid viscosities, as listed in Tables 2 and 3, respectively, were used in the simulation and considered in the discussion. The formation fluid was gas or oil and the injection fluid was oil, water, or SC-CO$_2$. SC-CO$_2$ is miscible with hydrocarbons and has a high diffusion coefficient. In the fracturing process, a pressurization stage occurs before crack initiation. At this pressurization stage, SC-CO$_2$ can fully dissolve with the formation fluid at the interface area. The interface between SC-CO$_2$ and hydrocarbon (gas or oil) disappears and the capillary force

decreases to zero. Before SC-CO$_2$ dissolves sufficiently into a formation fluid, the interfacial tension between SC-CO$_2$ and hydrocarbon is very small, approximately 2 mN/m (Li et al., 2017). The interfacial tension between water and hydrocarbon is approximately 50 mN/m. Thus, our simulation assumed that the capillary force between SC-CO$_2$ and the formation fluids (oil or gas) was negligible.

The inlet and outlet pressure values were derived from the fracturing experimental conditions of Zhang et al. (Zhang et al., 2017). In their experiment, the injection pressure was approximately 5 MPa after fracture initiation. Considering the pressure loss in tube, 4 MPa was used as the inlet pressure. However, 8 MPa was also set as the inlet pressure to ensure that the inlet pressure was higher than the threshold of the capillary force for different radii.

4. Validation

A validation of the flow model was conducted by comparing the analytical solutions in different flow situations: a) single-phase flow (the injection and formation fluids were the same); b) two-phase flow without considering the capillary force (*Pc*). The analytical solutions were based on the Buckley-Leverett theory (Buckley and Leverett, 1942; Idowu and Blunt, 2010). These solutions and the numerical results obtained from the flow model are plotted in Fig. 6. The numerical results of the single- and two-phase flows without capillary force were confirmed to be in good agreement with the analytical results derived from the homogeneous porous medium.

5. Simulation and results

To investigate the seepage effects of SC-CO$_2$ injection, five simulations were

conducted. Both capillary and viscous forces were integrated into the PNM to simulate the pressure field for a two-phase flow. The different injection conditions are listed in Table 4.

5.1 Effects of capillary force

The effects of capillary force on two-phase flow are presented in Fig. 7. The PNM-homo was used to simulate the effect of the capillary force. The constant pore-throat radius was set to $0.1 \, \mu m$. The results yielded snapshots of the pressure distributions derived from water injection with and without capillary force. Water was injected from the inlet (normalized length = 0). The case without Pc only considered the effect of viscous force, whereas that with Pc considered the effects of both capillary and viscous forces. When the capillary force was considered, a discontinuous pressure drop (DPD) occurred. The capillary force posed an extra resistant force to block the invasion of water. This resistant force derived from the capillary force could cause a DPD in the two-phase flow.

5.2 Effects of injection time

Water or SC-CO$_2$ injections were simulated in a homogeneous porous medium using PNM-homo. The constant average pore-throat radius was $0.1 \, \mu m$. The time variation of the pressure field is shown in Fig. 8. Water or SC-CO$_2$ was injected from the inlet (normalized length = 0), and the pressure field of the water injection, as shown in Fig.8(a), experienced a DPD that was caused by the capillary force. The injection fluid (water) was immiscible with the formation fluid (oil). When they met during injection, the capillary force was generated at the interface between water and

oil. With continuous injection, DPD continuously affected the pressure field. The positions of the DPD moved to the outlet side because of changes in the interfacial position between water and oil.

By contrast, the pressure field of the SC-CO_2 injection experienced no DPD, as shown in Fig. 8(b). Because SC-CO_2 and oil are miscible, no interface existed between them. In other words, no capillary force occurred between SC-CO_2 and oil, which means that no DPD occurred. Fig. 8(b) also shows that the slope of the pressure curve in the area displaced by SC-CO_2 (inlet side) was flatter than the area occupied by oil (outlet side). This was caused by both low viscous and low capillary forces of SC-CO_2, (i.e., the seepage effect). Because the injected SC-CO_2 penetrated into pores easily given a small pressure drop, pressure propagation was advanced with a value that approximated the injection pressure. The change points of slopes could be considered the interfacial positions between SC-CO_2 and oil. The interfacial position between SC-CO_2 and oil was ahead of that between water and oil. This indicated that the seepage effect of SC-CO_2 promoted the advancement of the interfacial front.

5.3 Effects of pore and throat radii

The influence of different pore-throat radii on the pressure field was investigated when considering the capillary and viscous forces using PNM-homo. The average pore-throat radii and corresponding permeability are listed in Table 5. These parameters were derived from the experiments with shale rocks (Lu et al., 2018). The sizes of simulation models for each pore radius are listed in Table 1.

Fig. 9(a) and (b) show the differences in the pressure fields between water and SC-CO_2 injections, respectively, in a homogeneous porous medium. Fig. 9(a) reveals

that the values of DPDs varied for the different average pore-throat radii. The DPD was influenced by the geometries of pore and throat. Because the DPD occurred as a result of the capillary force, the simulation results indicate that the capillary force could not be neglected due to the low permeability of rock when the injection fluid (water) was immiscible with the formation fluid (oil).

By contrast, with the SC-CO$_2$ injection, no DPD occurred, as shown in Fig. 9(b). The pressure field for the SC-CO$_2$ injection was controlled solely by the viscous force. Because of the low viscosity of SC-CO$_2$, the pressure distributions for different average pore-throat radii in small distances were nearly the same.

5.4 Heterogeneous porous medium

Rock for the most part is a heterogeneous porous media. Thus, investigating the pressure performances of water and SC-CO$_2$ injections in heterogeneous porous media is necessary. In our study, even the radius distributions were random, where the total average radius of the pore-throat for all pores and throats was $0.02\ \mu m$. The corresponding sample sizes are listed in Table 1.

A DPD occurred with water injection (Fig. 10(a)), but no DPD occurred with SC-CO$_2$ injection (Fig. 10(b)) in the heterogeneous porous medium. This indicated that the capillary and viscous forces affected the pressure fields in heterogeneous rocks. The results reveal that DPD clearly occurred when the injected fluid (water) was immiscible with the formation fluid (oil). For SC-CO$_2$, the property of miscibility with hydrocarbon produces a strong seepage effect.

5.5 Well injection with pre-existing fracture

Similar conditions as those in the experiment of Zhang et al. (Zhang et al., 2017)

were simulated using the PNM-frac. The formation fluid was assumed to be gas, which was intended to represent shale gas rock (hydrocarbon wet). The average pore-throat radius was set to 0.01 μm. The simulation results of pressure distributions for water and SC-CO_2 injections are presented in Fig. 11. The simulation results revealed that the DPD derived from the capillary force between water and gas blocked the spread of pressure (see Fig. 11(a)). However, in the case of SC-CO_2 injection, pressure spread easily without blocks because of the absence of capillary forces, as shown in Fig. 11(b). This indicated that the capillary force could cut off the pressure when the injection pressure was insufficient to overcome the threshold of the capillary force. It should be noted that the pore pressure in non-invaded elements in this model was set to 0 MPa.

5.6 Discussion of capillary force effect on the fracture geometry

In general, fracturing with water leads to tensile failure, which in turn generates fractures, and these fractures extend directly in the direction of the main stress. The simulation results for water injection suggested that the pressure spread was blocked by the capillary and viscous forces. However, the effect of capillary force on SC-CO_2 injection was negligible, and the viscous force for SC-CO_2 injection was lower than for water injection. The pressure could penetrate into the pore and throat around any pre-existing fracture. This can cause the pore pressure to increase considerably as compared with using water as injection fluid. When the pore pressure increased, the effective stress decreased. If we consider the Mohr-Coulomb failure criterion, shear failure events occur easily with a small effective stress (i.e., high pore pressure), as

shown in Fig.12(a). Therefore, increased pore pressure due to SC-CO$_2$ injection likely initiates shear failure cracks. Typically, a crack caused by shear failure is not parallel to a fracture caused by tensile failure (Labuz and Zang, 2012; Patton, 1966). Fracturing due to SC-CO$_2$ injection may lead to more branched and high tortuous fractures as well as rough fracture surfaces. Thus, the facture geometry derived from SC-CO$_2$ injection should be more complex than water injection because of shear failure cracks (see Fig. 12(b)). These inferred behaviors are consistent with the experimental results of Zhang et al., who showed that the fracture geometry of SC-CO$_2$ was more complex than water fracturing.

In fact, this paper is based on a flow model to study different pressure performances when injecting water and SC-CO$_2$. On this basis, combined with the Mohr-Coulomb failure criterion, it is concluded that SC-CO$_2$ fracturing should induce complex fractures. But this conclusion is not directly obtained through simulation. Therefore, in the following work, we will develop a solid model and couple it with the flow model to verify the aforementioned results that the fracture pattern induced by SC-CO$_2$ fracturing is complex fracture networks.

6. Conclusion

A two-phase steady-state flow model considering the effects of capillary and viscous forces was developed to investigate differences between aqueous and SC-CO$_2$ injections. The results of this study can be summarized as follows.

With respect to aqueous fluid injection, the pressure field was influenced by the capillary force because of immiscibility. The capillary force produced DPDs at the

interfacial points. The effects of capillary force on aqueous fluid were significant with respect to low-permeability reservoirs. However, miscible fluid such as SC-CO$_2$ reduced the effect of the capillary force and prevented DPD. Miscibility with hydrocarbon and the low viscosity of SC-CO$_2$ led to a strong seepage effect. The strong seepage effect of SC-CO$_2$ increased pore pressure in wide areas and induced shear fractures. This typically leads to the formation of complex fracture networks.

Acknowledgement

Author contributions

B. Liu planed and conducted the study. A. Suzuki contributed the design of the study. T. Ito contributed on the examination of the paper structure. All authors participated in the discussion and interpretation of results, as well as the writing of the manuscript.

Funding

Nomenclature

g conductance, $m^3/(\text{Pa.s})$;

L length of an element, m;

n number of corners;

z number of elements connecting to element i;

α_i half corner angle at corner i;

P pressure, Pa;

P_c capillary pressure, Pa;

q volumetric flow rate, m^3/s;

r the curvature radius of corner interface, m;

R inscribed radius of a cross-section, m;

Δt time-step size, s;

θ contact angle, radian;

σ interfacial tension between two fluid phases, N/m;

μ fluid viscosity, Pa $\cdot$ s;

V fluid volume in an element, m^3;

nw non-wetting phase;

w wetting phase;

C conductance of fluid in cross section, Pa.s/m^4

S_H, S_h Maximum principal stress and minimum principal stress

Reference

Aker, E., JØrgen MÅlØy, K., Hansen, A., Batrouni, G.G., 1998. A two-dimensional

network simulator for two-phase flow in porous media. Transp. Porous Media 32,

163–186. https://doi.org/10.1023/A:1006510106194

Al-Gharbi, M.S., 2004. Dynamic pore-scale modelling of two-phase flow. Imperial

College London.

Al-Gharbi, M.S., Blunt, M.J., 2005. Dynamic network modeling of two-phase

drainage in porous media. Phys. Rev. E - Stat. Nonlinear, Soft Matter Phys. 71,

1–16. https://doi.org/10.1103/PhysRevE.71.016308

Bakke, S., Øren, P.-E., 1997. 3-D Pore-scale modelling of sandstones and flow

simulations in the pore networks. SPE J. https://doi.org/10.2118/35479-PA

Belytschko, T., Organ, D., Gerlach, C., 2000. Element-free galerkin methods for

dynamic fracture in concrete. Comput. Methods Appl. Mech. Eng. 187, 385–399.

https://doi.org/10.1016/S0045-7825(00)80002-X

Bennour, Z., Ishida, T., Nagaya, Y., Chen, Y., Nara, Y., Chen, Q., Sekine, K., Nagano,

Y., 2015. Crack extension in hydraulic fracturing of shale cores using viscous oil,

water, and liquid carbon dioxide. Rock Mech. Rock Eng. 48, 1463–1473.

https://doi.org/10.1007/s00603-015-0774-2

Blunt, M.J., 2001. Flow in porous media - pore-network models and multiphase flow.

Curr. Opin. Colloid Interface Sci.

https://doi.org/10.1016/S1359-0294(01)00084-X

Buckley, S.E., Leverett, M.C., 1942. Mechanism of fluid displacement in sands. Trans.

AIME. https://doi.org/10.2118/942107-G

Choo, L.Q., Zhao, Z., Chen, H., Tian, Q., 2016. Hydraulic fracturing modeling using

the discontinuous deformation analysis (DDA) method. Comput. Geotech. 76,

12–22. https://doi.org/10.1016/j.compgeo.2016.02.011

Economides, M.J., Boney, C., 2000. Reservoir stimulation. Reserv. Stimul.

https://doi.org/10.1017/CBO9781107415324.004

Higdon, J.J.L., 2013. Multiphase flow in porous media. J. Fluid Mech.

https://doi.org/10.1017/jfm.2013.296

Hughes, R.G., Blunt, M.J., 2000. Pore scale modeling of rate effects in imbibition.

Transp. Porous Media 40, 295–322. https://doi.org/10.1023/A:1006629019153

Idowu, N.A., Blunt, M.J., 2010. Pore-scale modelling of rate effects in waterflooding.

Transp. Porous Media 83, 151–169. https://doi.org/10.1007/s11242-009-9468-0

Ishida, T., Chen, Y., Bennour, Z., Yamashita, H., Inui, S., Nagaya, Y., Naoi, M., Chen,

Q., Nakayama, Y., Nagano, Y., 2016a. Features of CO_2 fracturing deduced from

acoustic emission and microscopy in laboratory experiments. J. Geophys. Res.

Solid Earth 121, 8080–8098. https://doi.org/10.1002/2016JB013365

Ishida, T., Chen, Y., Bennour, Z., Yamashita, H., Inui, S., Nagaya, Y., Naoi, M., Chen,

Q., Nakayama, Y., Nagano, Y., 2016b. Features of CO_2 fracturing deduced from

acoustic emission and microscopy in laboratory experiments. J. Geophys. Res.

Solid Earth. https://doi.org/10.1002/2016JB013365

Joekar-Niasar, V., Hassanizadeh, S.M., 2012. Analysis of fundamentals of two-phase

flow in porous media using dynamic pore-network models: A review. Crit. Rev.

Environ. Sci. Technol. 42, 1895–1976.

https://doi.org/10.1080/10643389.2011.574101

Kantzas, Apostolos; Bryan Jonathan; Taheri, S., 2015. Fundamentals of fluid flow in

porous media 336.

Labuz, J.F., Zang, A., 2012. Mohr-Coulomb failure criterion. Rock Mech. Rock Eng.

https://doi.org/10.1007/s00603-012-0281-7

Latham, J., Guo, L., Wang, X., Xiang, J., 2011. Modelling the evolution of fractures

using a combined FEM-DEM numerical method. Harmon. Rock Eng. Environ. 449–454. https://doi.org/10.1201/b11646-77

Lecampion, B., Bunger, A., Zhang, X., 2017. Numerical methods for hydraulic fracture propagation: A review of recent trends. J. Nat. Gas Sci. Eng. https://doi.org/10.1016/j.jngse.2017.10.012

Liu, Q., Sun, L., Liu, P., Chen, L., 2018. Modeling simultaneous multiple fracturing using the combined finite-discrete element method. Geofluids 2018. https://doi.org/10.1155/2018/4252904

Lu, S., Li, J., Zhang, P., Xue, H., Wang, G., Zhang, J., Liu, H., Li, Z., 2018. Classification of microscopic pore-throats and the grading evaluation on shale oil reservoirs. Pet. Explor. Dev. 45, 452–460. https://doi.org/10.1016/S1876-3804(18)30050-8

Middleton, R., Viswanathan, H., Currier, R., Gupta, R., 2014. CO2as a fracturing fluid: Potential for commercial-scale shale gas production and CO2sequestration. Energy Procedia 63, 7780–7784. https://doi.org/10.1016/j.egypro.2014.11.812

Mogensen, K., Stenby, E.H., 1998. A dynamic two-phase pore-scale model of imbibition. Transp. Porous Media 32, 299–327. https://doi.org/10.1023/a:1006578721129

Nguyen, V.H., Sheppard, A.P., Knackstedt, M.A., Val Pinczewski, W., 2006. The effect of displacement rate on imbibition relative permeability and residual saturation. J. Pet. Sci. Eng. 52, 54–70. https://doi.org/10.1016/j.petrol.2006.03.020

Øren, P.E., Bakke, S., 2003. Reconstruction of Berea sandstone and pore-scale

modelling of wettability effects. J. Pet. Sci. Eng.

https://doi.org/10.1016/S0920-4105(03)00062-7

Øren, P.E., Bakke, S., 2002. Process based reconstruction of sandstones and

prediction of transport properties. Transp. Porous Media.

https://doi.org/10.1023/A:1015031122338

Patton, F.D., 1966. Multiple modes of shear failure in rock. 1st Int. Congr. Rock

Mech.

Peng, P., Ju, Y., Wang, Y., Wang, S., Gao, F., 2017. Numerical analysis of the effect

of natural microcracks on the supercritical CO_2 fracturing crack network of shale rock

based on bonded particle models. Int. J. Numer. Anal. Methods Geomech.

https://doi.org/10.1002/nag.2712

Piri, M., Blunt, M.J., 2005. Three-dimensional mixed-wet random pore-scale network

modeling of two- And three-phase flow in porous media. I. Model description.

Phys. Rev. E - Stat. Nonlinear, Soft Matter Phys. 71, 1–30.

https://doi.org/10.1103/PhysRevE.71.026301

Reynolds, C.A., Blunt, M.J., Krevor, S., 2018. Multiphase Flow Characteristics of

Heterogeneous Rocks From CO_2 Storage Reservoirs in the United Kingdom.

Water Resour. Res. https://doi.org/10.1002/2017WR021651

Shi, F., Wang, X.L., Liu, C., Liu, H., Wu, H.A., 2017. An XFEM-based method with

reduction technique for modeling hydraulic fracture propagation in formations

containing frictional natural fractures. Eng. Fract. Mech. 173, 64–90.

Shimizu, H., Murata, S., Ishida, T., 2011. The distinct element analysis for hydraulic

fracturing in hard rock considering fluid viscosity and particle size distribution.

Int. J. Rock Mech. Min. Sci. 48, 712–727.

https://doi.org/10.1016/j.ijrmms.2011.04.013

Valvatne, H., 2004. Predictive pore-scale modelling of multiphase flow 146.

Vilarrasa, V., Bolster, D., Dentz, M., Olivella, S., Carrera, J., 2010. Effects of CO_2

compressibility on CO_2 storage in deep saline aquifers. Transp. Porous Media.

https://doi.org/10.1007/s11242-010-9582-z

Wang, S., Feng, Q., Dong, Y., Han, X., Wang, S., 2015. A dynamic pore-scale

network model for two-phase imbibition. J. Nat. Gas Sci. Eng. 26, 118–129.

https://doi.org/10.1016/j.jngse.2015.06.005

Watanabe, N., Egawa, M., Sakaguchi, K., Ishibashi, T., Tsuchiya, N., 2017. Hydraulic

fracturing and permeability enhancement in granite from subcritical/brittle to

supercritical/ductile conditions. Geophys. Res. Lett. 44, 5468–5475.

https://doi.org/10.1002/2017GL073898

Yan, C., Zheng, H., Sun, G., Ge, X., 2016. Combined finite-discrete element method

for simulation of hydraulic fracturing. Rock Mech. Rock Eng. 49, 1389–1410.

https://doi.org/10.1007/s00603-015-0816-9

Zhang, X., Lu, Y., Tang, J., Zhou, Z., Liao, Y., 2017. Experimental study on fracture

initiation and propagation in shale using supercritical carbon dioxide fracturing.

Fuel 190, 370–378. https://doi.org/10.1016/j.fuel.2016.10.120

Zhao, Q., Lisjak, A., Mahabadi, O., Liu, Q., Grasselli, G., 2014. Numerical simulation

of hydraulic fracturing and associated microseismicity using finite-discrete

element method. J. Rock Mech. Geotech. Eng. 6, 574–581.

https://doi.org/10.1016/j.jrmge.2014.10.003

1
2
3
4
5
6
7
8
9
10
11
12
13
14
15
16
17
18
19
20
21
22
23
24
25
26
27
28
29
30
31
32
33
34
35
36
37
38
39
40
41
42
43
44
45
46
47
48
49
50
51
52
53
54
55
56
57
58
59
60
61
62
63
64
65

The seepage effect estimation model for supercritical CO_2 and water fracturing in unconventional gas reservoir is proposed.

The simulation results show that capillary force has strong effect on seepage effect.
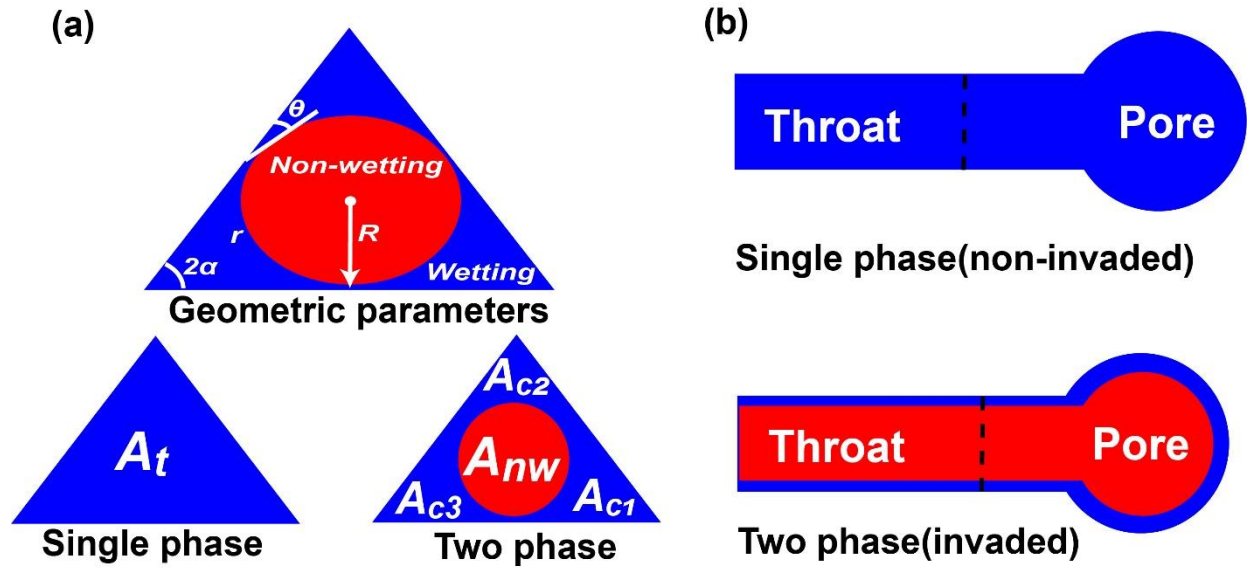
Figure

Fig. 1. Schematic image of configuration.
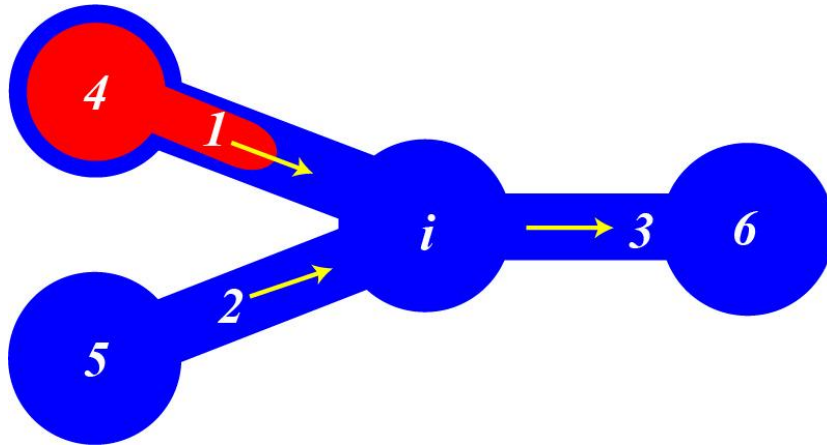
Fig. 2. Schematic diagram of volume flux conversation. The yellow arrows represent the flow direction.
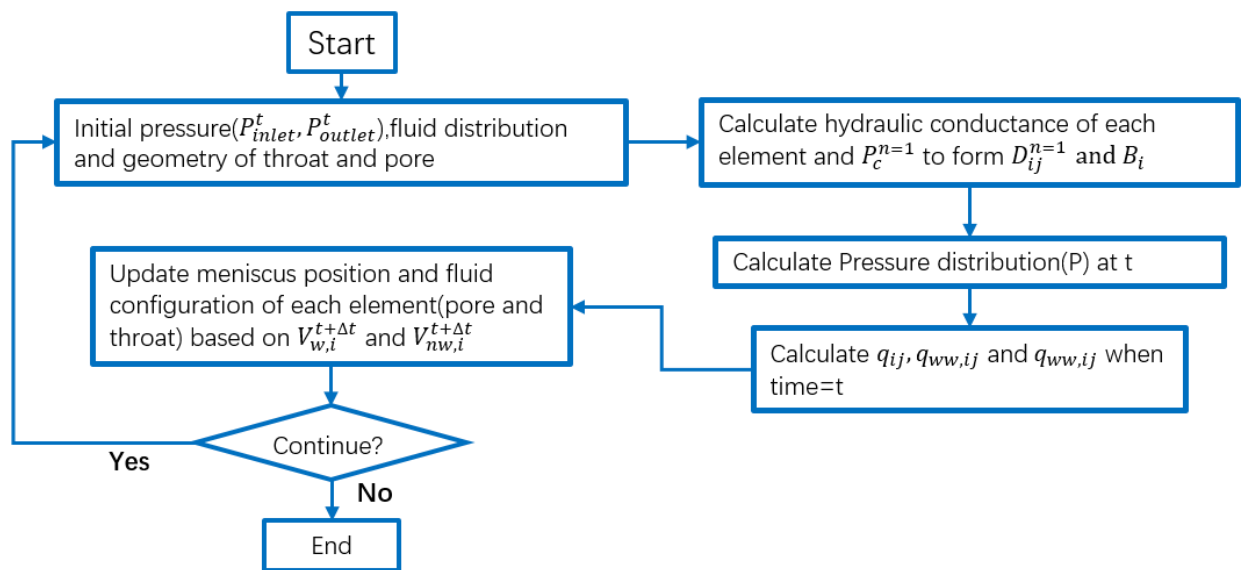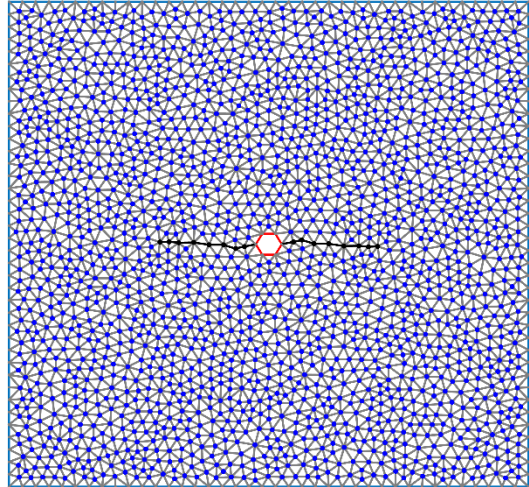
Fig. 3. Computational procedure.
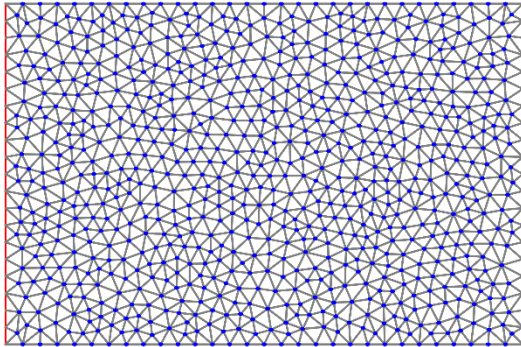
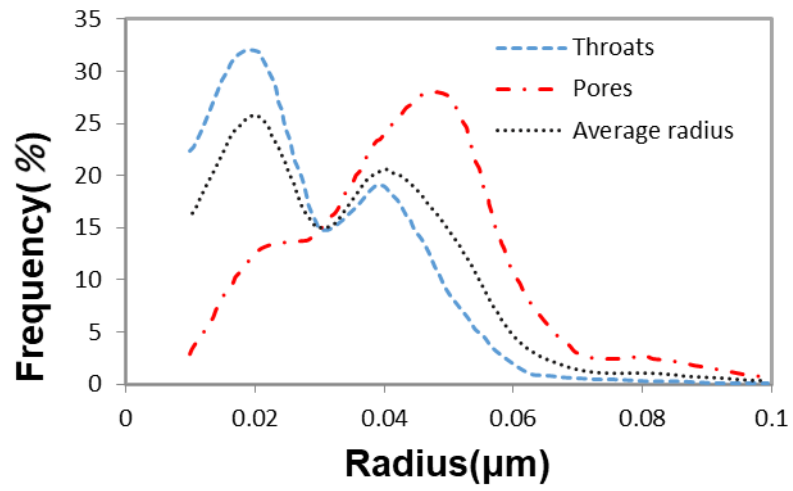**Fig. 4.** Structure of pore network for simulation.

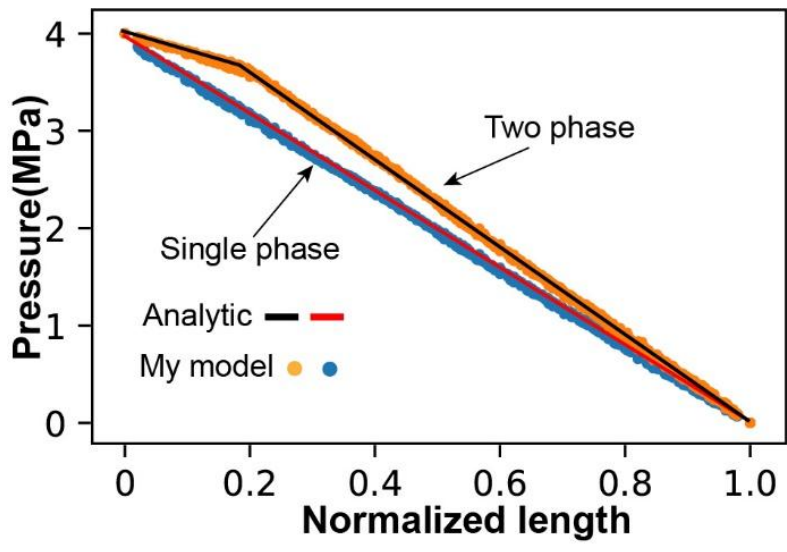**Fig. 5.** Pore and throat size distributions for heterogeneous porous medium (PNM-hetero).
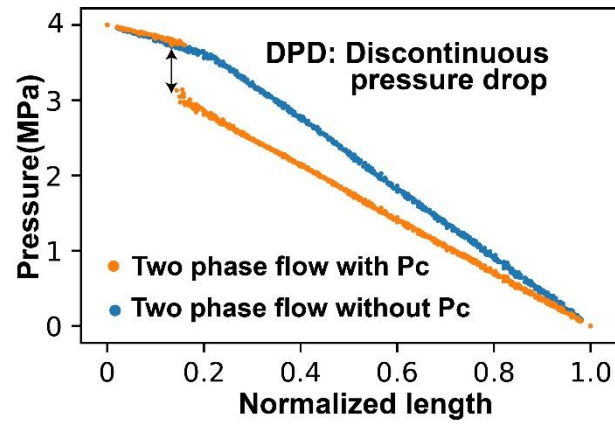
Fig. 6. Validation of flow model using PNM-homo.

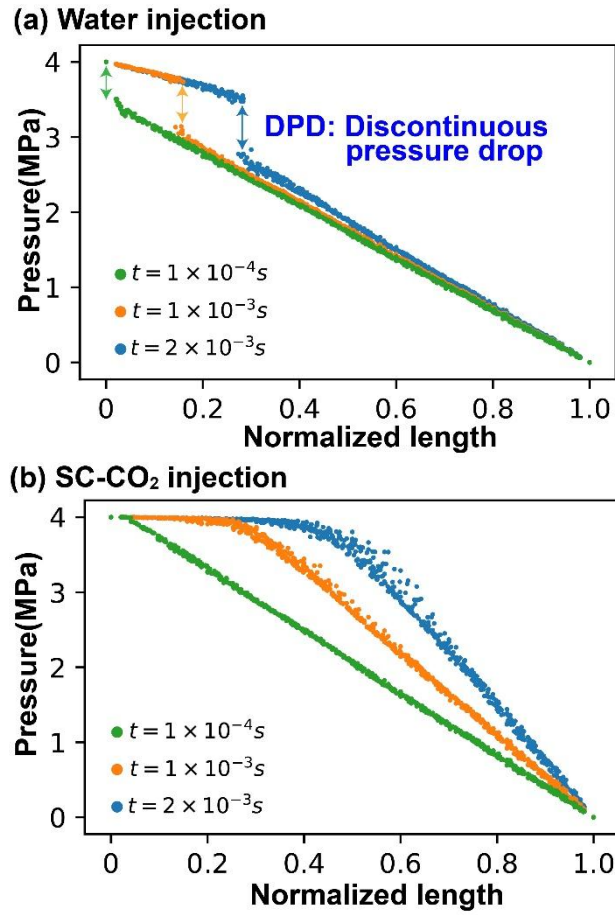**Fig. 7**. Effect of capillary force on pressure field using PNM-homo.

(a) Water injection

(b) SC-CO₂ injection

Fig. 8. Pressure field of different injection time using PNM-homo.
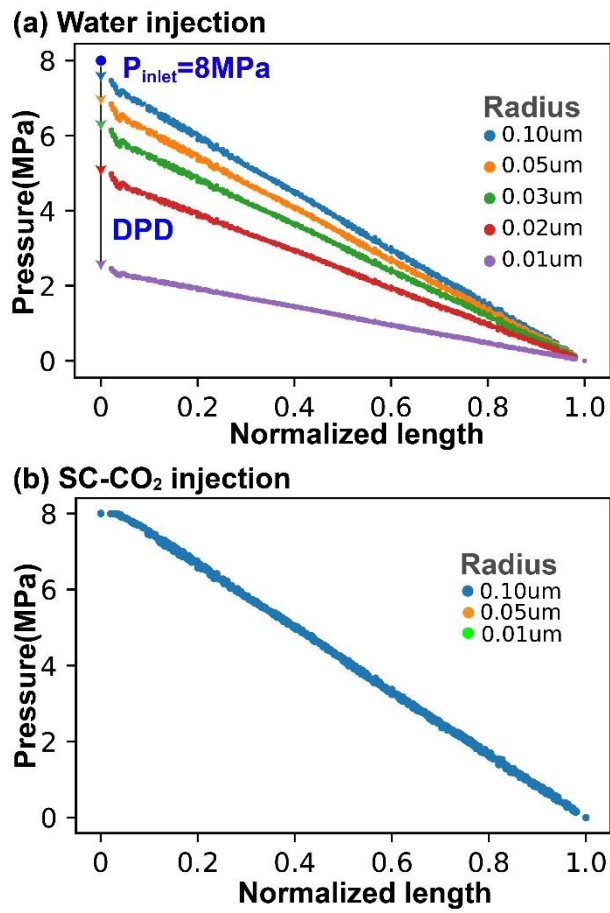
Fig. 9. Pressure field of different pore-throat ~~radius~~ using PNM-homo.

(a) Water injection
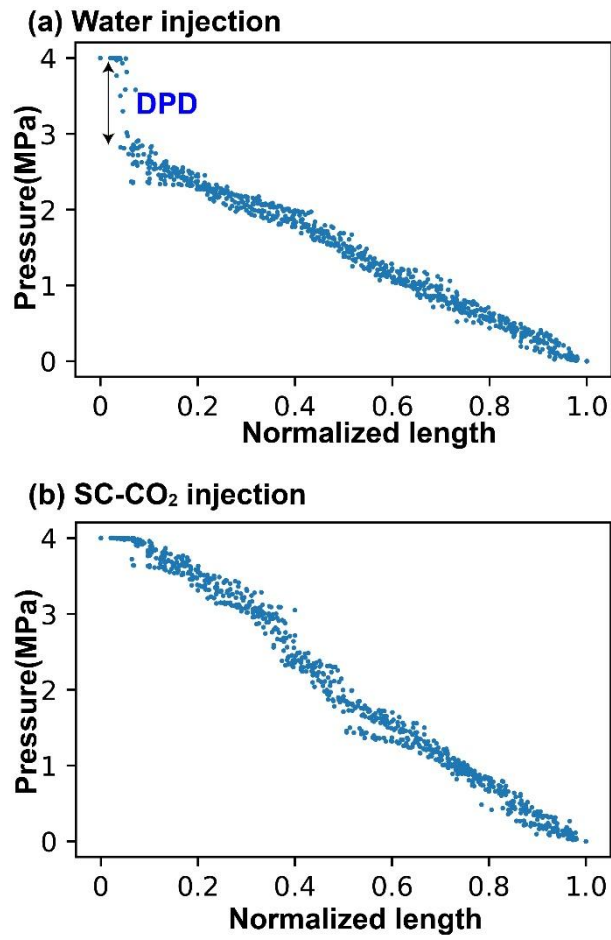

(b) SC-CO₂ injection

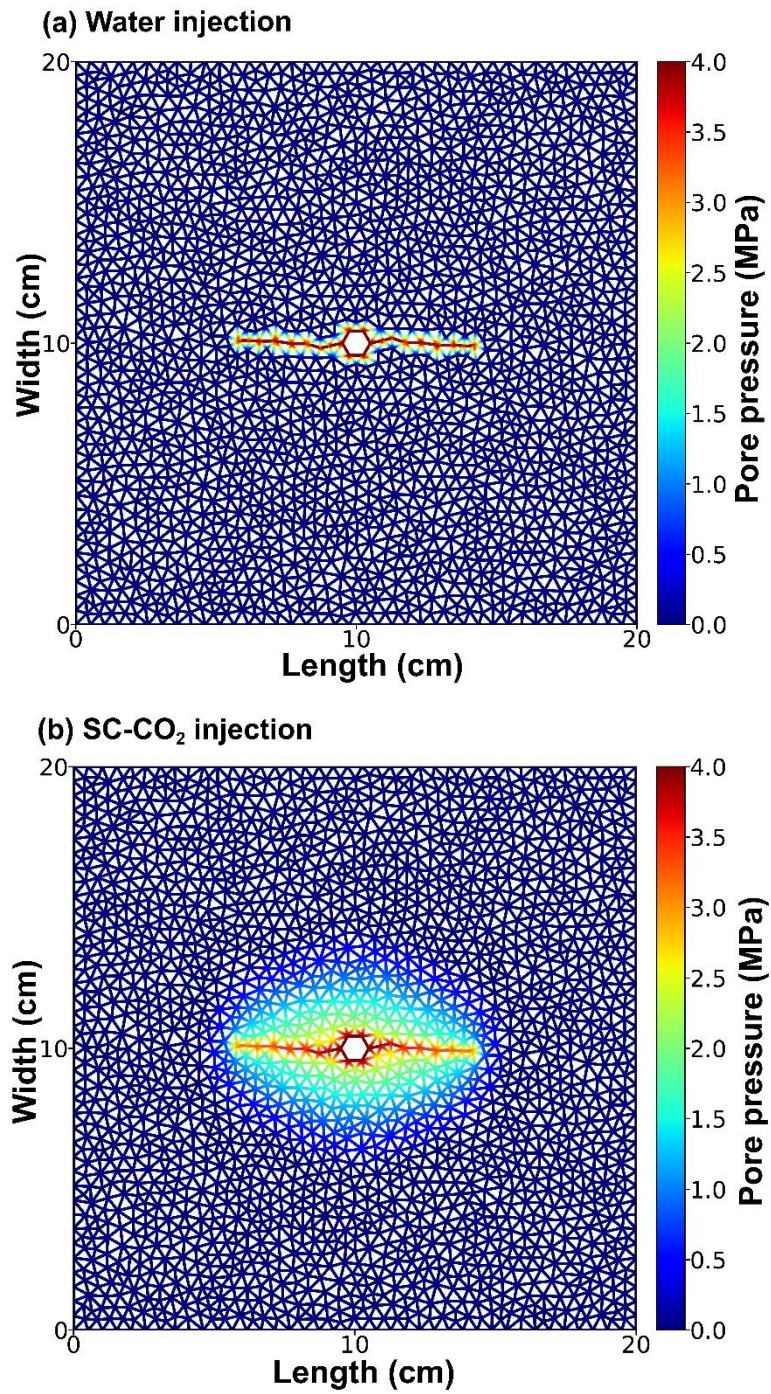**Fig. 10.** Pressure field of two-phase flow considering capillary force using PNM-hetero.

Fig. 11. Pressure field due to water injection and SC-CO$_2$ injection in homogenous porous medium with pre-existed fractures using PNM-frac.

(a) Mohr-Coulomb failure criterion

τ

SC-CO$_2$ Water

σ

Pore pressure increasing

(b) Geometry of fracture

Dry shale rock
Formation fluid is air

$P_c \neq 0$
(Water)

$P_c = 0$
(SC-CO$_2$)
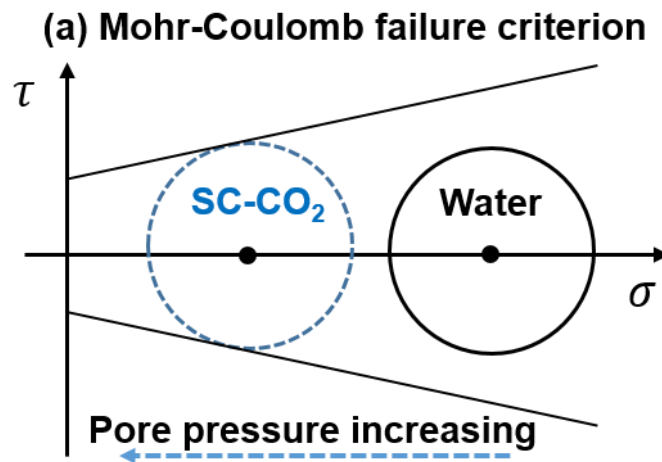
Fig. 12. **(a)** Schematic diagram of Mohr-Coulomb failure criterion and **(b)** geometry of different type of fractures.

Table 1 Simulation sample size and average radius of pore-throat.

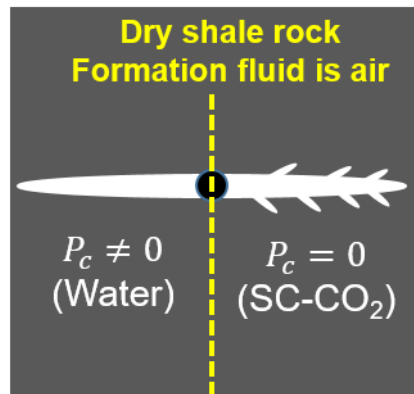| Simulation sample	Average pore-throat radius (μm)	Size of model ($mm \times mm$)
1	0.15	0.225×0.15
2	0.10	0.150×0.10
3	0.05	0.075×0.05
4	0.03	0.045×0.03
5	0.02	0.030×0.02
6	0.01	0.015×0.01

Table 2 Fluid systems for simulation.

Fluid system (injection - formation)	Contact angle (deg)	Interfacial tension (mN/m)
Water-Gas	0	50.0
SC-CO_2-Gas	Miscible	Miscible
Water - Oil	30	30
SC-CO_2 -Oil	Miscible	Miscible

Table 3 Fluid viscosity.

Fluid	Viscosity ($mPa \cdot s$)
Gas	0.011
Water	0.89
Oil	4.0
SC-CO_2	0.02

Table 4 Simulation cases.

Simulation	Injecting fluid	Formation fluid	Inlet pressure (MPa)	Outlet pressure (MPa)	Injection time (10^{-4}s)	Network
Validation	Oil/Water	Oil	4.0	0	2.0	PNM-homo
5.1	Water	Oil	4.0	0	2.0	PNM-homo
5.2	Water/SC-CO$_2$	Oil	4.0	0	1.0-20	PNM-homo
5.3	Water/SC-CO$_2$	Oil	8.0	0	2.0	PNM-homo
5.4	Water/SC-CO$_2$	Oil	4.0	0	2.0	PNM-hetero
5.5	Water/SC-CO$_2$	Gas	4.0	0	1200	PNM-frac

Table 5 Classification of shale oil reservoirs.

Classification	Permeability ($10^{-3}\mu m^2$)	Average pore-throat radius (μm)
I	> 1	> 0.15
II	1~0.4	0.15~0.07
III	0.40~0.05	0.01~0.07
IV	< 0.05	< 0.01